JOURNAL OF PROPULSION AND POWER
Vol. 36, No. 5, September–October 2020

Optically Resolved Fuel Regression of a Clear Polymethylmethacrylate Hybrid Rocket Motor

Flora S. Mechentel,* Blake R. Hord,† and Brian J. Cantwell‡
Stanford University, Stanford, California 94305

https://doi.org/10.2514/1.B37805

A novel fuel regression measurement technique was developed using a single-port, clear polymethylmethacrylate (PMMA) grain and a high-resolution camera, providing temporally and spatially resolved data in a small-scale hybrid motor. By visualizing the fully illuminated port through a flat PMMA surface, the fuel grain diameter can be measured along the axial dimension. This paper provides the details of the implementation, data processing, validation, and results from 21 hotfires. A wide range of operating conditions were tested by varying the initial diameter, the fuel grain length, the oxidizer mass flow rate, and the precombustion chamber length. The main difficulty associated with this technique is correcting the data to account for the change in index of refraction of the solid PMMA as heat soaks into the material surrounding the port. Qualitative and quantitative data can be extracted to further improve our fundamental understanding of hybrid combustion and upgrade motor designs. This new regression method is nonintrusive, low cost, and easy to implement, and it has the potential to provide reliable space–time-dependent data for laboratory-scale motors.

Nomenclature

a, n	=	empirical coefficients for flux-based regression rate law
d_{aft}	=	optically resolved aft-end port diameter
d_{pi}	=	initial port diameter
G	=	total mass flux through the port
L_f	=	fuel grain length
L_{post}	=	postcombustion chamber length
L_{pre}	=	precombustion chamber length
m_f	=	burned fuel mass
$\dot{m}_{\text{ox}}$	=	oxidizer mass flow rate
n	=	index of refraction
OF	=	oxidizer-to-fuel ratio
r	=	radius
T	=	temperature
T_{amb}	=	ambient temperature
T_g	=	glass transition temperature
t	=	time
t_b	=	burn time
x	=	distance from the fore-end of the grain
α	=	thermal diffusivity
ρ	=	density

Subscripts

corr	=	corrected with thermal model
opt	=	measured optically
w	=	port wall

I. Introduction

IN a time of increasing demand of small-scale commercial satellite deployments and a push for more cost-efficient interplanetary exploration missions, the need for safe and low-cost micropropulsion options is clear. Over the past two decades, trade studies have shown that hybrid motors are a promising alternative to mono- or bipropellant motors capable of delivering relatively high Δv (on the order of 1 km/s) for small-satellite maneuvers [1,2]. However, a main limitation (and source of uncertainty) in these preliminary designs is the solid fuel regression rate and its dependence on the oxidizer flow and the motor geometry. Space–time-averaged data are typically deduced from the fuel mass differential before and after a firing, and used to determine the empirical coefficients for a flux-based law. However, complete reconstruction of the instantaneous performance of the motor based on endpoint measurements can lead to large errors, especially for long-duration firings and configurations with large spatial variations in the burn profile. As a result, preliminary design studies fail to gain significant traction, because they rely heavily on common assumptions and empirically derived data, which can vary widely from one experimental apparatus to another.

The development of low-cost, high-accuracy, and nonintrusive techniques to measure spatially and temporally resolved data is of high interest in hybrid rocket development. An extensive overview of measurement techniques can be found in [3]. However, there is no method to date that has provided a full set of spatially and temporally resolved port dimensions with high accuracy. Ultrasound sensors have been used for instantaneous, single-point measurements, but do not provide a complete reconstruction of the fuel profile with time [4]. De Zilwa et al. [5] measured the instantaneous port diameter by measuring the Helmholtz frequency with a fast-response signal from a pressure transducer. However, only the spatially averaged diameter can be derived with this technique, and uncertainties are especially introduced in configurations with large oxidizer-to-fuel ratio shifts or high nozzle erosion rates. X-ray radiography has successfully been used to derive complete data sets, but the associated cost and ease of implementation can deter from using it in academic research environments [6]. Furthermore, the accuracy of the method still requires more investigation. As a result, the hybrid community still suffers from the lack of a widely used and reliable measurement method to fully investigate motor ballistics.

Optical diagnostics have not commonly been used for regression rate measurements. Nevertheless, DeLuca et al. developed a time-resolved technique capable of following the quasi-steady ballistics of solid fuels in cylindrical grains with a central perforation in a two-dimensional radial microburner [7]. The regression rate was performed by a visual technique tracking the gasifying surface of the

Presented as Paper 2019-4192 at the AIAA Propulsion and Energy 2019 Forum, Indianapolis, IN, August 19–22, 2019; received 10 September 2019; revision received 24 March 2020; accepted for publication 28 March 2020; published online 27 April 2020.

*Ph.D. Candidate, Department of Aeronautics and Astronautics, 496 Lomita Mall. Member AIAA.

†Undergraduate Student, Department of Aeronautics and Astronautics, 496 Lomita Mall. Member AIAA.

‡Edward C. Wells Professor, Department of Aeronautics and Astronautics, 496 Lomita Mall. Fellow AIAA.

fuel grain during combustion. Narsai [8] implemented a transparent window at the fore-end of a cylindrical gaseous oxygen/paraffin wax motor through which images of the port were acquired. The light contrast between the combustion products and the solid fuel was high enough to apply a threshold filter to the captured images and determine the hydraulic diameter of the port using a low-cost, high-speed camera (512×384 resolution at 300 frames per second). However, it only provided fore-end regression data, and acquisition time was limited by soot deposition on the window during the burn. This research and other activities considering clear polymethylmethacrylate (PMMA) for preliminary design studies of a small-satellite thruster inspired the development of a new technique for fuel regression measurements.

This paper describes the development of a cost-efficient, nonintrusive, and easy-to-implement optical measurement technique for hybrid motors. Details regarding the experimental apparatus and the image processing method are described. Using results from 21 hot-fires, efforts were put toward validating the data and modeling causes for uncertainty. Finally, the instantaneous and spatially resolved fuel regression data are briefly compared with a commonly used regression rate model for hybrid rocket motors.

II. Experimental Setup

The details of the experimental setup used for this investigation have already been described in [9], and component drawings are provided in [10]. An 8.9-cm-thick (3.5-in.-thick) PMMA grain with a square cross section and a single circular port is placed between two stainless steel components with face seals, and held in compression with four tie rods. All of the fuel grains used in this study were machined out of a single 3 m^2 sheet of commercially available PMMA (procured from Professional Plastics, Inc.) with two parallel and optically transparent surfaces. By using an optically clear fuel and no thermal insulation or protective casing, it was expected that the edge of the internal port surface during the burn could be tracked with a high-resolution camera. A picture of the assembly is given in Fig. 1.

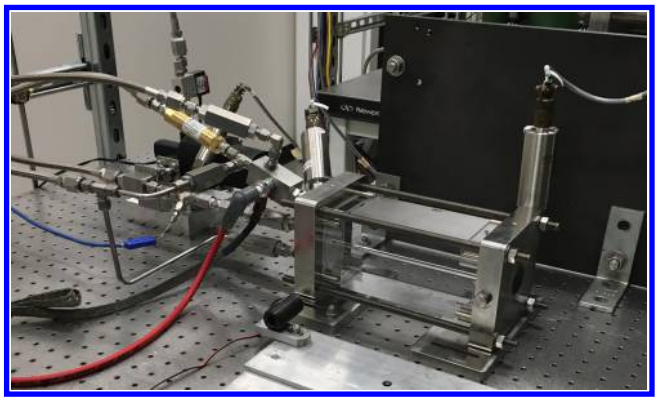

Fig. 1 Picture of the laboratory-scale motor with direct optical access for high-resolution imaging of the port.

The motor design provides full-length visual access to the internal port. A Panasonic HC-X1000 Video Camcorder was selected because of its high-resolution capability (3840×2160) at 60 frames per second (progressive). This affordable camera also features an integrated neutral density filter (up to 1/64) and a 20× zoom, allowing it to be placed far away from the burning fuel to reduce perspective distortion. However, placing the object far away from the camera makes it more difficult to install it perfectly parallel to the sensor. This can introduce some amount of error, especially with a shallow depth of field. A dot target was used to characterize the setup, and the image was reduced to the field of view of interest (approximately 3500×900 pixels). The largest distortion was observed at the far right of the image, where it also appeared slightly less in focus. This suggested that there was a small angle between the camera sensor and the dot target. Nevertheless, the vertical distortion at the far right of the image was only 0.6 mm (less than 0.6%) with respect to the center. More details can be found in [10].

The error associated with the fuel regression measurement is dependent on the quality of the images captured. The camera settings (aperture, shutter speed, sensor sensitivity [ISO], white balance) ultimately define the amount of postprocessing required to extract useful data. With this technique, the objective is to obtain a sharp contrast between the hot combustion products in the port and the surrounding solid fuel. The first set of tests produced reflections and a blurry port surface, most likely due to diffraction at small apertures. Efforts were put into installing a black neutral background, carefully setting the focus before installing the grain using a target grid, and reducing the light reaching the sensor with a wide aperture. This was achieved by reducing the exposure time to 0.5–1 ms. At these shutter speeds, the port is fully saturated and produces the desired contrast at the solid boundary, as shown in Fig. 2.

III. Data Processing

With the ideal settings achieved, a robust edge detection scheme was implemented with a threshold filter and a globally calculated limit using Otsu's method (MATLAB function *imbinarize*). Assuming

Fig. 2 Edge detection with ideal camera settings. The fuel port edge is resolved with a globally determined threshold and visible on the postprocessed image.

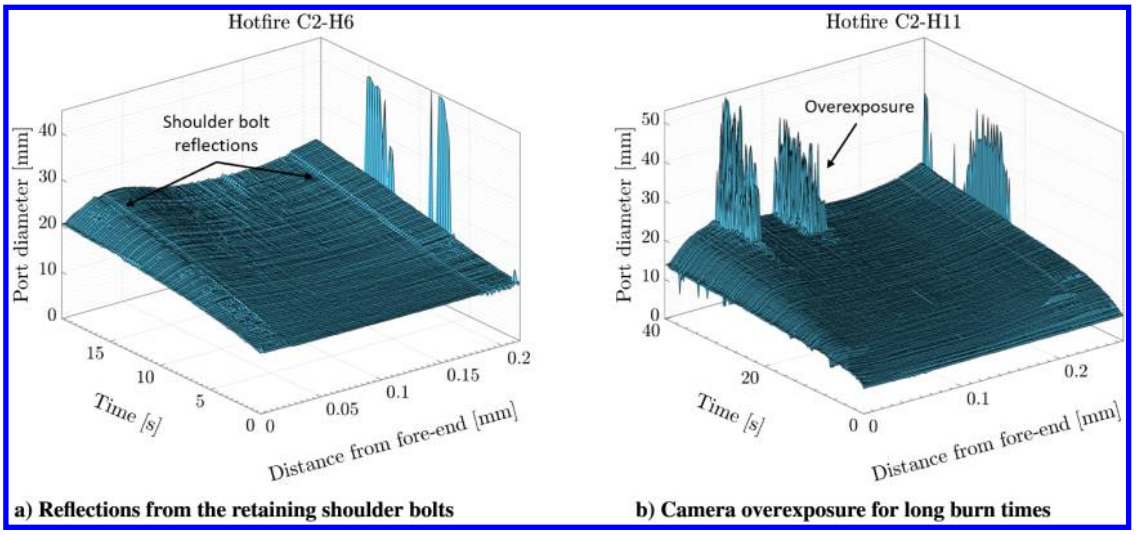

Fig. 3 Three-dimensional representation of the port diameter versus distance from the fore-end and time, illustrating certain optical aberrations in two different hotfires.

axisymmetry of the central perforation, the number of pixels between the top and bottom boundaries in each column determine the port diameter, which is then converted to a true dimension through calibration before the firing. Depending on the length of the fuel grain, and therefore the size of the field of view, one pixel corresponded to 50–70 microns. Each frame provides a complete fuel profile, but the associated noise severely increases at the fore- and aft-ends of the grain. Figure 2 shows the original image and the port edge in red in the postprocessed image. The black arrows point to consistent aberrations due to reflections on metal shoulder bolts constraining the fuel grain. A tip of a shoulder bolt is indicated with a green arrow.

As the fuel port opens up radially, the cross-sectional area increases, allowing more light to reach the camera. As a result, the image brightness increases with time. However, because the camera is set to obtain a fully illuminated port, the exposure is very close to saturation. For long burn times, the light source from the combustion becomes too strong and the fuel is eventually illuminated beyond the port surface. The edge can ultimately no longer be resolved. The overexposure starts in areas of high regression, i.e., more hot combustion products and larger cross-sectional areas, and eventually progresses to the entire port length. This problem limited the test time and rendered certain data sets unusable in the last seconds of firing. Ideally, the exposure time would need to be changed throughout the burn to optimize the data output. Alternatively, the motor could be restarted at a later time with a different camera setting. In fact, the regression rate measurement taken over multiple restarts coincided extremely well with continuous hotfire measurements. More details on the subject can be found in [10].

The measured regression data are best represented using a three-dimensional plot with the fuel length scale on the x axis, time on the y axis, and fuel port diameter on the z axis. This is a direct way to visualize aberrations such as those created by the shoulder bolts, or loss of the edge due to overexposure. Examples are shown in Fig. 3. The hotfire nomenclature is defined with the campaign number (C2) and the hotfire number (H1–21), and the operational conditions of each test are given in Appendix Table A1.

IV. Data Validation

The objective is to determine if the port diameter measured as a function of time and space with the optically resolved method corresponds to the "true" port diameter during the burn. To do so, a high-resolution picture of the fuel grain was taken after each firing. Ideally, a redundant instantaneous measurement would need to be acquired for direct comparison.

A. Postfiring Images

The first step was to validate that the postfiring image taken after complete cooldown and processed with the correct pixel-to-dimension conversion corresponded to the final fuel port profile. It is relatively common in hybrid motor analysis to split the fuel grain into two halves to get optical access to the lengthwise cross section of the fuel. However, this method can lead to large errors if the cut is slightly offset from the true diameter or the tool removes a relatively large amount of material. Instead, the fuel grain was cut perpendicular to the port axis at different locations, resulting in seven fuel "slices." The pieces were machined to obtain flat parallel surfaces (except the fore- and aft-ends) and the axial locations of the faces were carefully recorded. This enabled port diameter measurements at 14 different positions along the grain axis. However, the diameter could not be well resolved at the fore- and aft-ends, resulting in a total of 12 axial positions used for the comparison. A picture of the seven fuel slices is shown in Fig. 4.

The port diameter was measured with calipers. Additionally, each flat face of the slice was imaged with a 4800-dpi scanner to obtain high-resolution pictures of the circular port at the different axial locations (Fig. 5). The relative errors between the diameters obtained with the postfiring image of the grain and the "true diameters" (taken as the average of the caliper measurements and the scans of the fuel slices) were less than 1%, which is of the same order as the uncertainty associated with the true diameter determination (taken as the average of the caliper measurement and the value derived from the scans). As a result, there were no measurable optical distortion effects after the burn, and it was determined that the postfiring images could be used to measure the final fuel grain profile.

B. Comparison of the Final Hotfire Frame and the Postfiring Image

To determine if the edge found during the burn actually corresponds to the fuel port surface, the profile obtained with the last frame with a saturated port was compared with the postfiring image. This process is illustrated in Fig. 6. Figure 6c shows that the edge at the end of the firing and the edge after cooldown are distinct. As a matter of fact, this observation was made consistently across all 21 firings: the diameter obtained with the final fully illuminated frame always underestimated the port diameter measured after cooldown. Additionally, the discrepancy was on the same order of magnitude as the difference in the burned fuel mass (6–10%), measured with a weighing scale and calculated with the final port dimension from the images.

To better quantify this effect, the camera was set to the maximum zoom setting to increase the image resolution over the field of view of interest for a dedicated test. A roughly 10-cm section of the fuel grain (approximately 50% of the total length) was filmed during the firing and cooldown. The results of the process described in the previous paragraph are shown in Fig. 7. This test not only demonstrated that the port profile resolved at the end of the firing was systematically smaller than the profile obtained after the cooldown, but the video also showed that the optical properties of the material changed drastically right after the motor shutdown. Additionally, a thin layer below the fuel surface

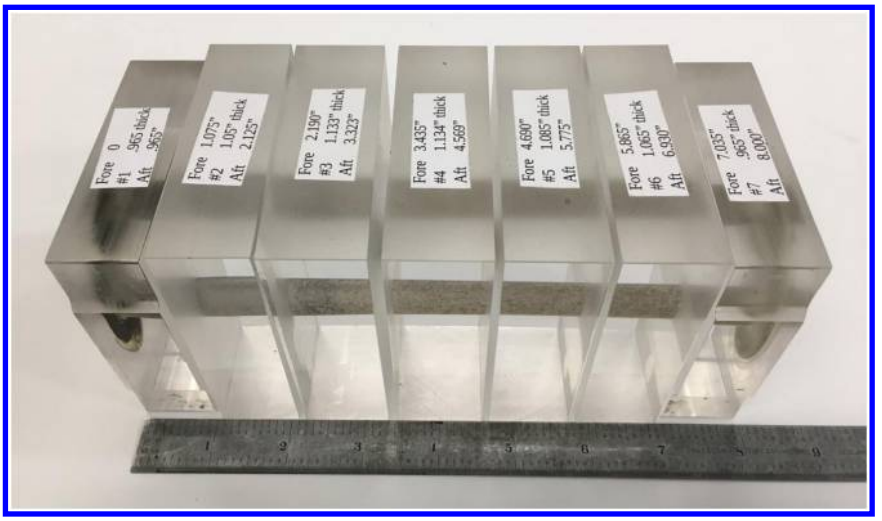

Fig. 4 Fuel slices machined for port diameter measurements at different axial positions (hotfire C1-H9).

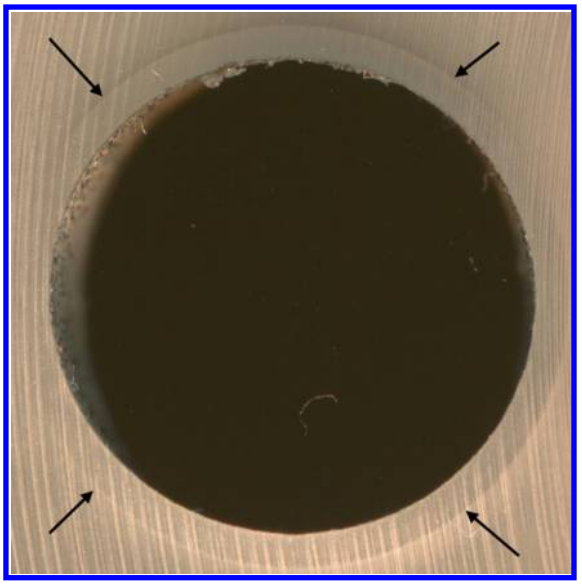

Fig. 5 Image of the face of a fuel slice obtained with a 4800 dpi scanner.

was observed and presented a different refractive index than the rest of the PMMA. It was difficult to obtain a clear image of this effect, but it is indicated with white arrows in Fig. 7. With the correct lighting conditions, this layer was also observed on the scans of the fuel grain slices, as indicated with the black arrows in Fig. 5.

C. Summary

The process of comparing the final test frame and the postfiring image was repeated for 11 hotfires, and the difference between the two edges was calculated and averaged over the length of the grain, excluding the fore- and aft-ends (due to noisy measurements). The relative difference in port diameter was consistently between 5 and 8%, regardless of the initial dimension. The high-resolution (maximum zoom) test showed a relative difference of 7.9%. Four hypotheses were considered to explain this discrepancy: 1) the fuel continues to pyrolize after the flame is extinguished; 2) the nitrogen purge displaces a layer of molten fuel off the surface; 3) the fuel expands as heat penetrates during the firing and contracts as a result of cooling after the motor shutdown; 4) the change in refractive index during the firing is significant enough to bend the light rays emanating from the port and distort the image.

The first hypothesis seems unlikely because the regression rate (between 0.1 and 0.3 mm/s) would drastically decrease without the presence of the flame to maintain the fuel temperature above the degradation temperature at the surface. This effect alone would not explain a discrepancy of about 1 mm on the diameter as was observed over many tests. The second hypothesis was ruled out by testing without purging with nitrogen after closing the oxygen valve. This made no significant change to the diameter difference. Furthermore, if a layer of molten fuel was displaced with the flow of nitrogen, PMMA residues would most likely be found around the convergent section of the nozzle. The following section will address the third and fourth hypotheses.

V. Data Correction

This section is dedicated to presenting the modeling efforts put in place to understand the systematic error observed between the port diameter measured with the last firing image and the diameter measured after cooldown. Because this effect is inherently related to the material properties, a brief overview of some thermochemical characteristics of PMMA is first provided.

A. Material Properties of PMMA

PMMA is a completely amorphous polymer, meaning that is has no crystalline structures and the long chains of repeated monomer ($C_5H_8O_2$) have a disordered formation. Because crystals can scatter light, the absence of crystalline structures is what gives the acrylic polymer its exceptional transparency. Glass transition is a property of the amorphous portion of the solid, and so PMMA only exhibits a glass transition temperature (T_g) around 100°C and no melting temperature.

The ambient-temperature density of commercial PMMA was obtained with helium pycnometry[§] and measured at 1183 kg/m^3. The scale had a reported precision of ± 1 mg and the sample volume was measured by gas displacement with a relative uncertainty of $\pm 0.3\%$, leading to an overall density precision of ± 4 kg/m^3. This uncertainty was obtained by theoretical error propagation using the random relative uncertainties of the pressure measurements for the gas displacement. However, independent measurements of two different PMMA samples using this method only displayed a 0.5 kg/m^3 difference, suggesting that the error propagation method provides a conservative estimate of the overall uncertainty. Bywater and Toporowski [11] determined the specific volume–temperature curves of different PMMA samples using a density gradient column up to 160°C. The specific volume variation of relatively atactic samples was linear with temperature and presented a slope change at the glass transition temperature. The experimental data suggest that the density can be determined with the following function (with T in K and ρ in kg/m^3):

$$\rho = \begin{cases} 1000(0.000246 \times T + 0.77)^{-1} & T \le T_g \\ 1000(0.000568 \times T + 0.65)^{-1} & T \ge T_g \end{cases} \quad (1)$$

[§]This work was performed in the Stanford Rock Physics Laboratory (SRPL) in the Department of Geophysics.

Fig. 6 Comparison of the port edges obtained with the final test frame and the postfiring image (C2-H7).

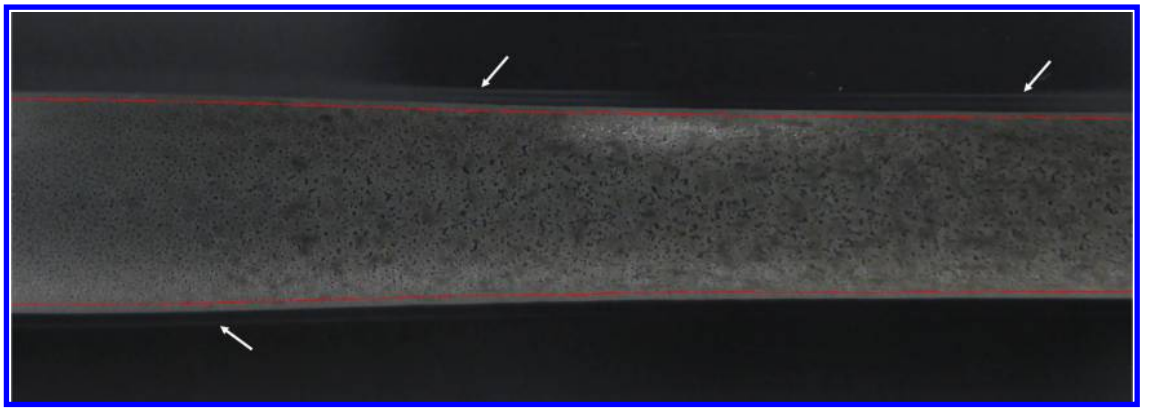

Fig. 7 Edge obtained with the last firing image overlaid on a postfiring image of the fuel at high resolution (C1-H10).

Another property of interest is the variation of index of refraction with temperature. Michel et al. [12] measured the refractive index using the prism method and monitored the temperature with a thermocouple fastened in the sample. The samples were annealed to relieve preexisting stresses, and the samples were heated with a maximum rate of 0.2°C/ min up to 150°C (before the material softens), and without applying any stress. The variation follows a linear behavior with a slope change around the glass transition temperature, similar to the density variation with temperature. The refractive index of PMMA can therefore be described with the following equation (with T in K):

$$n = \begin{cases} -0.000130 \times T + 1.53 & T \leq T_g \\ -0.000313 \times T + 1.60 & T \geq T_g \end{cases} \tag{2}$$

The density and refractive index variations with temperature are shown in Fig. 8, assuming a glass transition temperature at the intersection of the two linear portions (approximately 100°C).

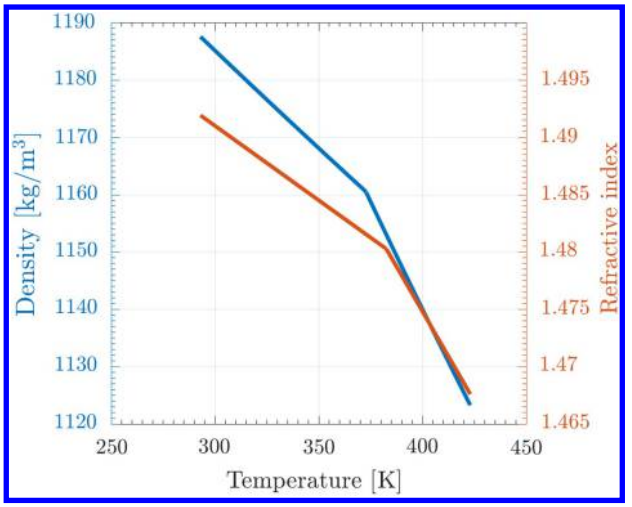

Fig. 8 Thermal variation of density (blue) and index of refraction (orange) of PMMA derived from data in [11] and [12].

B. Thermal Modeling

To estimate the error associated with the effects that could explain the discrepancy in the diameter at the end of the burn (thermal contraction/expansion or ray distortion), a one-dimensional thermal model was implemented. For a more detailed analysis, refer to reference [10]. The model is quasi steady in the sense that it does not consider any startup transients. The heat equation in cylindrical coordinates with a constant-wall-temperature boundary condition is (with $\alpha \approx 0.11 \times 10^{-6}$ m^2/s for PMMA [13])

$$\begin{cases} \alpha \dfrac{\partial^2 T}{\partial r^2} + \dfrac{\alpha}{r}\dfrac{\partial T}{\partial r} = \dfrac{\partial T}{\partial t} \\ T(r = r_w, t) = T_w \\ T(r \to \infty, t) = T_{\text{amb}} \\ T(r > r_w, t = 0) = T_{\text{amb}} \end{cases} \tag{3}$$

To simplify the problem, the spatial variable is redefined as $\hat{r} = r - r_w$ to account for advection of the regressing port surface. The domain is defined as a series of concentric rings around the fuel surface, and central discretization schemes are used for the spatial variables. A first-order scheme is used for the time derivative. Assuming a constant surface temperature (estimated between 300 and 500°C), the thermal profile below the surface can be numerically resolved for different regression rate values. Figure 9 shows that the higher the regression rate, the thinner the thermal penetration layer.

Shlensky et al. [14] demonstrated that a limiting heating temperature exists in the thermal decomposition of polymers, and that above this temperature, the material can no longer absorb energy, but decomposes and vaporizes as molecular fragments. For PMMA, the limiting temperature of pyrolysis is conservatively 500°C. Above this temperature, it is therefore inconsistent to use material properties for PMMA because the virgin material has already undergone thermal degradation. Figure 10 shows the thermal profile in the material for different surface temperatures and the thermal penetration depth, defined as the fuel thickness where $T > T_{\text{amb}}$. Results suggest that this thickness is not very sensitive to T_w for the conditions of interest.

C. Thermal Expansion and Contraction

From Eq. (1), the density of the fuel under the surface can be estimated assuming that the linear variation remains valid beyond the experimental range tested (150°C). This substantial extrapolation is the biggest limitation in the model. However, it is expected that this assumption would lead to conservative estimates of the error associated with thermal expansion and contraction of the fuel grain. The effects of chamber pressure are neglected and the density variation is illustrated in Fig. 11.

Fuel mass loss per unit length during the burn is calculated with the varying density profile. Conservation of mass at the end of the burn is used to calculate the diameter of the grain after cooldown where

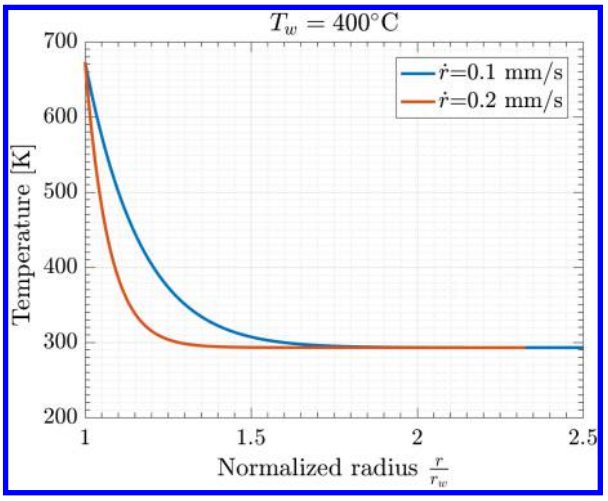

Fig. 9 Numerical solution of the thermal profile in the fuel grain at $t = 20$ s with a prescribed wall temperature $T_w = 400$°C.

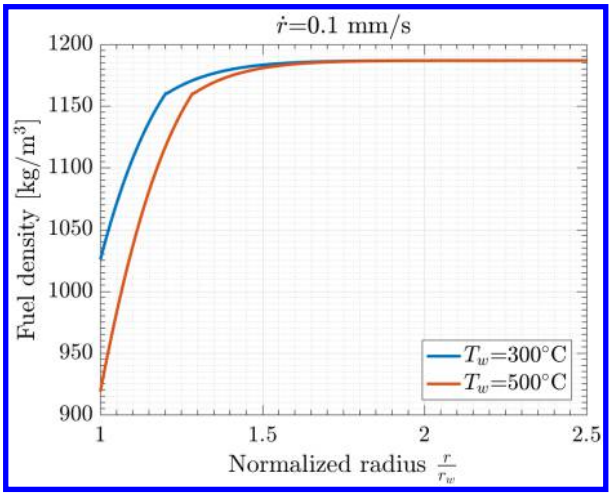

Fig. 11 Density profile below the fuel surface as a function of surface temperature.

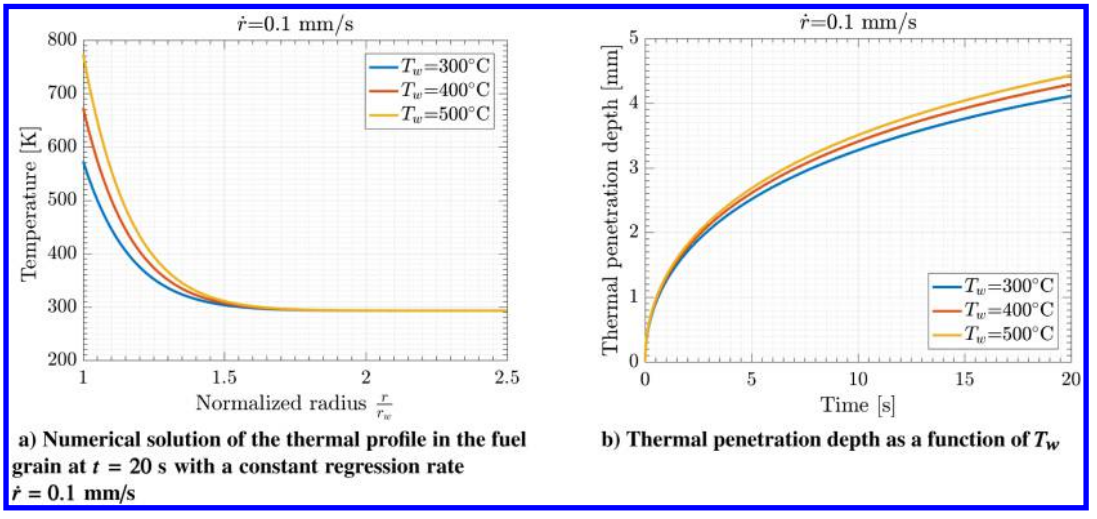

a) Numerical solution of the thermal profile in the fuel grain at $t = 20$ s with a constant regression rate $\dot{r} = 0.1$ mm/s

b) Thermal penetration depth as a function of T_w

Fig. 10 Numerical solution of the thermal profile and penetration depth in the fuel grain varying the surface temperature.

$T = T_{amb}$. The widest density variation is observed for low regression rates, high surface temperature, and long burn times. For $\dot{r} = 0.1$ mm/s, $T_w = 500$°C, and $t_b = 30$ s, the diameter difference due to thermal contraction at the end of the burn was less than 0.4 mm for the two initial port diameters tested. Despite the conservative assumptions made in this analysis, the error observed in the fuel port diameter estimation at the end of the burn (over 1 mm on average) could not be explained with density effects alone.

D. Optical Distortion

The observation of a change of refractive index in the material below the fuel surface led to the assumption that the light rays emanating from the burning fuel port were bent before reaching the camera sensor, leading to a systematic error in the diameter estimation. A representative schematic is given in Fig. 12, where the ray bends as a result of the decrease in index of refraction with temperature (Fig. 8). The camera is located about 1.5 m away from the fuel grain, and the port diameter has a maximum value of 25 mm, so that the vertical angular view of the camera is about

$$2 \times \tan^{-1}\left(\frac{0.025}{2 \times 1.5}\right) < 1^{\circ}$$

This justifies the assumption of parallel rays reaching the camera and not being refracted at the PMMA–air interface. A tangent effect must also be considered because the ray emanating from the true diameter would need to traverse inside the fuel port to exit the grain horizontally. As a result, the ray emanates from the point (x_1, y_1) shown in Fig. 12.

Using Snell's law at each boundary interface and various geometrical considerations, the numerical solution for the optical distortion can be derived from the results of the thermal model previously described. Correction results for the time-varying radius are given in Fig. 13. However, the prescribed surface temperature affects the refractive index profile and therefore the corrected radius. It was shown that the relative difference quickly reaches an asymptotic behavior after 5 s with $((|r_{corr} - r_{opt}|)/r_{opt}) = 5$–$10\%$ for surface temperatures varying from 300 to 500°C. As a result, the relative offset measured with the postfiring image can be applied as a correction to the time-varying data for each hotfire. As a reminder, the relative difference between the optically measured diameter at the end of the burn and the diameter after cooldown was experimentally found between 5 and 8%, which is within the range predicted by this model.

The most important takeaway from this simulation is that the relative difference between corrected and experimental data can be considered constant throughout the burn after the establishment of the thermal layer, and the experimental data can be corrected with a constant multiplicative factor. As a result, the relative offset measured with the postfiring image can be applied as a correction to the time-varying data for each hotfire.

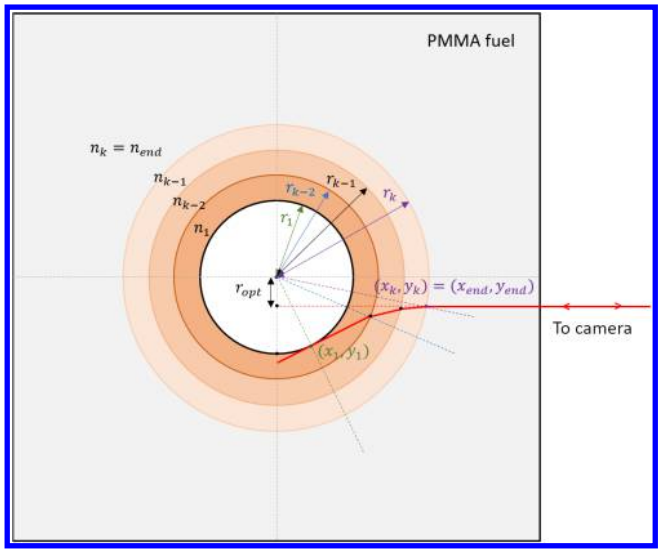

Fig. 12 Schematic of optical distortion due to refractive index changes within the solid fuel.

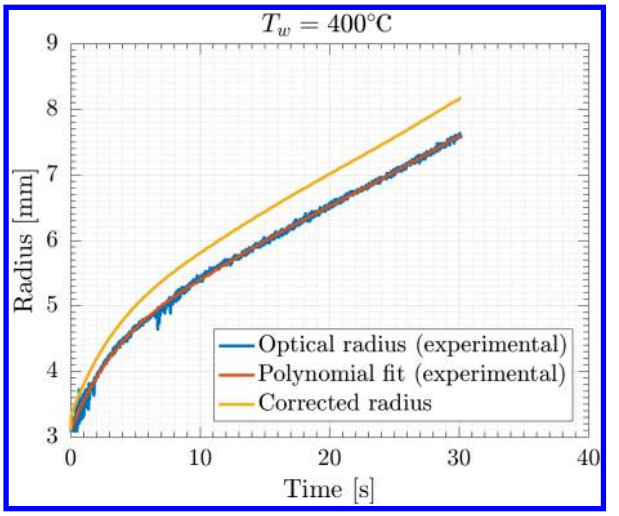

Fig. 13 Refractive index correction applied to experimental data assuming a constant surface temperature $T_w = 400$°C.

VI. Additional Considerations

A. Spatial Averaging

Conventional regression rate laws assume a cylindrical fuel grain throughout the burn. The optically resolved data give a unique opportunity to estimate the error made when spatially averaging the port diameter. In fact, the test conditions led to large variations along the length of the grain. An example is shown in Fig. 14, where the port radius as a function of time is plotted at different axial locations and the coefficient of variation (standard deviation/mean) is calculated at each time step. All of the data sets presented this type of behavior for the coefficient of variation: the port becomes less cylindrical with time, with maximum deviations up to 15% of the mean.

To calculate the fuel mass burned as a function of time, the density is assumed constant, and the volume change is converted to a mass loss at each time step. Even though the radius deviates significantly from the mean along the length of the grain, the fuel mass burned calculated with the x-dependent data and the spatially averaged radius were nearly identical. These results were consistent across all the tests and strongly suggest that as long as an average port radius can be modeled, the fuel mass flow rate can be estimated without simulating the entire spatially dependent regression. The complete modeling remains useful to estimate fuel residuals and avoid burning through thermal insulation. However, the difficulty lies in developing a spatially averaged fuel regression rate model given these strong axial variations. For example, the fuel grain length will have a large impact on the average port radius for the same operating conditions, suggesting that a simple flux-based law with constant coefficients is insufficient to capture these effects. Further supporting this assumption, Kumar and Ramakrishna [15] found a strong length-to-diameter dependence in regression rate coefficients.

B. Numerical Differentiation

In preliminary designs, regression rate is required to estimate the fuel mass flow rate, but the actual measured quantity is the port radius as a function of time. To obtain the regression rate, a direct approach is to numerically differentiate between data points. Although this works very well with smooth curves, it can be impractical for experimental data subject to noise and spurious errors. Before differentiating, the data can be processed by smoothing, interpolating, or curve fitting. All of these data reduction methods can lead to very different derivative estimations, especially near the endpoints. In particular, curve fitting

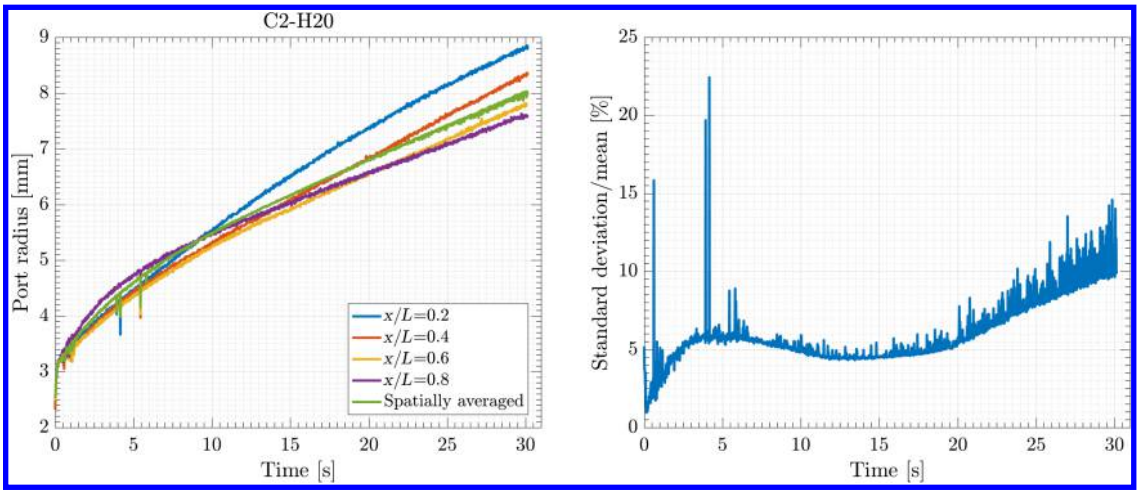

Fig. 14 Results of spatial averaging for a typical test (C2-H20).

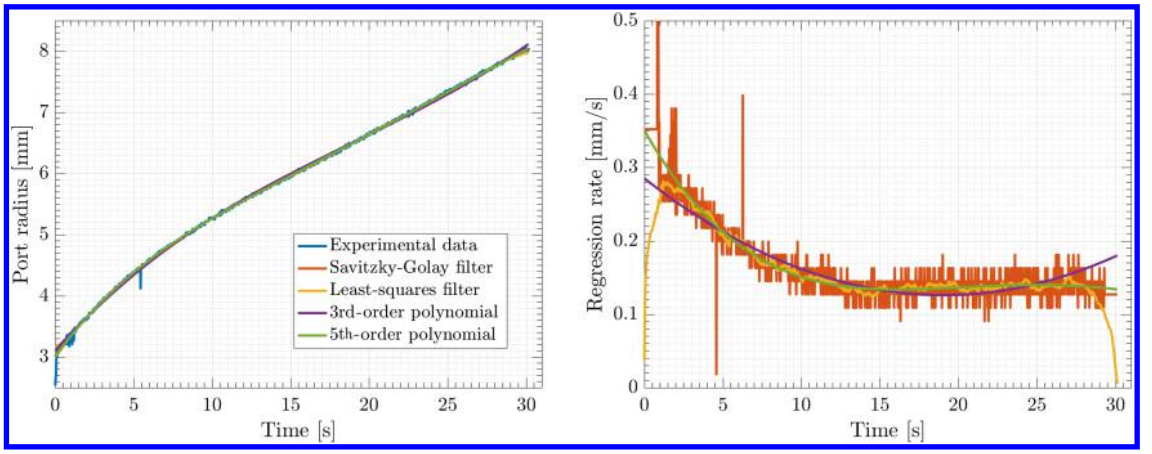

Fig. 15 Smoothing/curve fitting and numerical differentiation.

can be extremely useful to work with smooth data, but it presupposes the behavior of the derivative, which can introduce significant errors. Figure 15 displays certain smoothing or fitting methods (and their parameters), and the drastic differences in resulting regression rate. It is extremely rare to find details of data reduction from port dimensions to regression rate in the literature describing instantaneous measurements taken on hybrid motors (e.g., in [16]). This difficulty was recognized by Gramer and Taagen [17], who tried to fit their experimental data through integration instead.

The different smoothing and curve fitting methods do an excellent job at representing the experimental data. Although the different regression rates follow the same general trend, the endpoints are the hardest to estimate correctly. For example, the third- and fifth-order polynomials give a regression rate difference over 20% at the beginning and end of the firing.

C. Regression Law

The most common regression rate law used in hybrid rocket analysis and design is the Marxman's diffusion-limited model ($\dot{r} = a_0 G^{n_0}$) [18]. Using the regression rate law as a function of the total mass flux G leads to two coupled, first-order partial differential equations for the port radius and the total mass flow rate flowing through the port, as a function of x and t [19]. To simplify the problem, the regression rate law is commonly rewritten as a function of the oxidizer mass flux G_{ox}, so that the equation can be integrated analytically. The empirical coefficients a and n in Eq. (4) were solved for each experimental data set using the corrected instantaneous optical radius (averaged over the length of the grain) by least-squares minimization. This was accomplished with the MATLAB function *lsqnonlin* including the constraint $0.1 < n < 0.9$. An example of the fit is shown in Fig. 16.

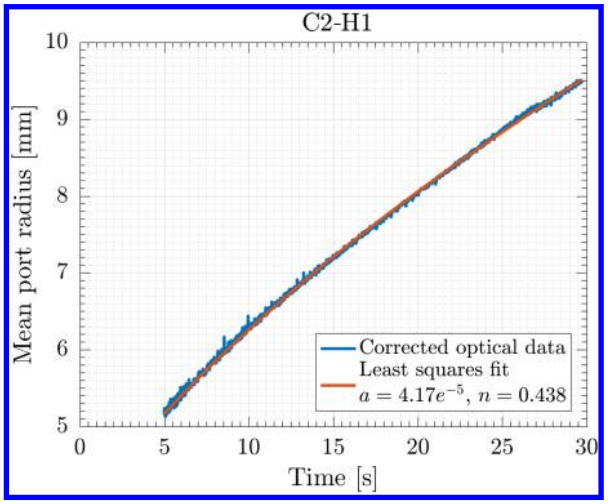

Fig. 16 Corrected optical radius averaged over the fuel length fit to the classical regression rate law for a gaseous oxygen (GOX)–PMMA combination.

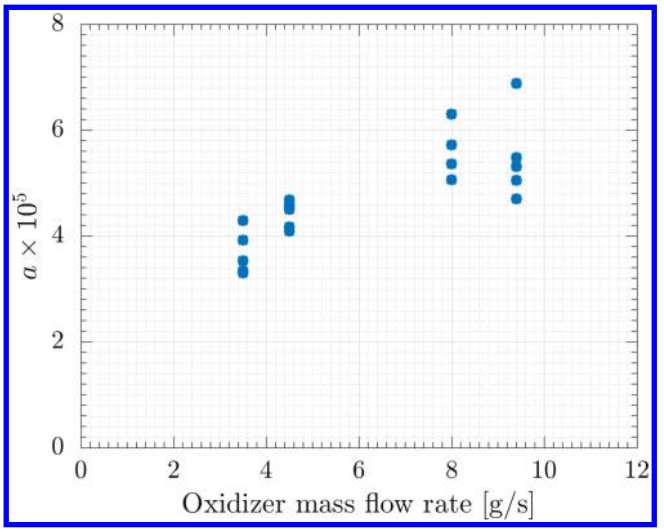

Fig. 17 a coefficients (from the classical regression rate law $\dot{r} = aG_{ox}^n$) solved for each test using the corrected instantaneous optical radius (averaged over the length of the grain) by least-squares minimization, plotted as a function of oxidizer mass flow rate.

$$\begin{cases} \dot{\bar{r}} = aG_{ox}^n = a\left(\frac{\dot{m}_{ox}}{\pi \bar{r}^2}\right)^n \\ \bar{r}(t) = \left[\bar{r}(0)^{2n+1} + (2n+1)a\frac{\dot{m}_{ox}^n}{\pi^n}t\right]^{1/(2n+1)} \end{cases} \tag{4}$$

This method was applied to 20 hotfires (data available in [10]). The mean n across all the tests was 0.442 with only a 4% variation. The a coefficient, however, varied by over 19%. This hints to the fact that a is a strong function of experimental conditions, which could also explain the wide disparity of values in the literature. Unfortunately, 20 data sets were not enough to completely decouple all experimental conditions, but a closer analysis of the a values demonstrated a strong correlation with the oxidizer mass flow rate (Fig. 17), although other experimental conditions (fuel grain length, precombustion chamber length) could also have an influence. This ultimately means that even though the fuel mass flow rate can be estimated very well with the spatially averaged radius, the spatial variations affect the value of $\bar{r}$, especially when the burn time is long (over 20 s). It is believed that the injection scheme also has a large influence on the regression rate, and more details can be found in reference [20].

VII. Conclusions

A novel experimental method for measuring solid fuel regression rate in a hybrid motor was developed and is referred to as the "optically resolved fuel regression technique." Using an optically clear fuel and a high-resolution camera, the port edge was detected with a simple threshold filter when the appropriate camera settings were chosen to acquire the ideal contrast between the burning port and the surrounding fuel. This low-cost and easy-to-implement measurement technique provides space- and time-dependent data currently lacking in the literature. However, the instantaneous measurements would need to be validated with a redundant method such as ultrasound sensing. Although the technique is only applicable to optically clear fuels such as PMMA or polycarbonate, it has value for fundamental research in hybrid rocket ballistics.

The final port diameter measurements were compared with a postfiring picture of the fuel grain and presented a systematic discrepancy. It was determined that the optically resolved technique led to an underestimation of the true port diameter due to a change in the index of refraction of the material below the surface as heat soaked into the material. A thermal model with a constant wall temperature condition was developed to validate this theory. The results were in good agreement with the order of magnitude of the error, with a surface temperature assumption consistent with results found in the literature. The error was found to remain constant throughout the burn, and the acquired port radius data could be corrected with a multiplicative constant between 5 and 8%.

Caution is raised when using port regression data to determine the regression rate of the fuel. In fact, different numerical smoothing or fitting methods before differentiation can introduce large errors. Integrating a regression rate law to fit the experimental data is the preferred method. However, fits to the $\dot{r} = aG_{ox}^n$ model were inadequate and confirm that the fuel regression over long burn times, with large axial variations in the regression, and for different internal motor geometries is not well modeled by this expression. Although n only varied by 4% across 20 hotfires, a varied by over 19% for the same propellant combination, suggesting that this law does not capture all the required physics for detailed modeling.

Appendix

Table A1 Hotfire operating conditions for the 21 hotfires of campaign 2

Test	d_{pi}, in.	$\dot{m}_{ox}$, g/s	L_f, in.	L_{pre}, in.	L_{post}, in.	t_b, s	m_f, g	OF	d_{opt}, cm	d_{aft}, cm
1	0.25	4.5	8.45	0.25	0.25	29.8	64.5	2.1	1.91	1.82
2	0.25	4.5	8.45	0.25	0.25	9.3/9.4/9.1	21.9/18.4/18.4	1.9/2.3/2.2	N/A	N/A
3	0.25	4.5	8.45	0.75	0.25	28.7	65.4	2.0	1.95	1.97
4	0.25	4.5	8.45	1.25	0.25	29.3	68.9	1.9	2.00	1.92
5	0.50	9.4	8.45	1.25	0.25	19.4	77.2	2.4	2.40	2.52
6	0.50	9.4	8.45	0.75	0.25	19.8	75.1	2.5	2.37	2.41
7	0.50	9.4	8.45	0.25	0.25	19.3	67.8	2.7	2.26	2.26
8	0.50	9.4	8.45	1.25	0.25	19.6	73.6	2.5	2.31	2.22
9	0.25	4.5	8.45	1.25	0.25	29.5	73.8	1.8	2.02	2.22
10	0.25	3.5	8.45	0.25	0.25	30.1	55.0	1.9	1.79	1.78
11	0.25	3.5	10.45	0.25	0.25	40.2	89.9	1.6	2.07	2.38
12	0.25	4.5	10.45	0.25	0.25	35.4	98.4	1.6	2.16	2.54
13	0.25	3.6	6.45	0.25	0.25	30.2	47.7	2.3	1.94	1.76
14	0.25	4.5	6.45	0.25	0.25	30.3	55.2	2.5	2.08	1.88
15	0.50	9.3	10.45	1.25	0.25	19.7	97.9	1.9	2.46	2.61
16	0.50	8.1	10.45	1.25	0.25	19.7	85.9	1.8	2.37	2.50
17	0.50	8.1	8.45	1.25	0.25	19.4	67.8	2.3	2.36	2.39
18	0.50	8.1	8.45	1.25	0.75	19.3	66.0	2.4	2.35	2.37
19	0.50	8.1	8.45	1.25	1.25	19.6	64.5	2.4	2.29	2.26
20	0.25	3.5	8.45	0.25	1.25	30.1	52.0	2.0	1.78	1.79
21	0.25	3.5	8.45	0.25	1.25	30.4	55.0	1.9	1.88	2.05

Acknowledgments

The research was funded by the Stanford School of Engineering Dean's Office. The Ph.D. candidate conducting this research was also supported through the Stanford Graduate Fellowship and the Zonta Foundation Amelia Earhart Fellowship. The undergraduate student was supported through the Stanford Research Experience for Undergraduates program. The authors would like to warmly thank Greg Zilliac and Nicolas Lee for their insightful reviews and discussions. Appreciation is extended to Brian Carilli, Godwin Zhang, Renee Quiroz, Richard Maggi, Richard Lam, Jon Mohs, and Kevin Manalili for all their work and commitment that led to the development of the testing facility and acquisition of these experimental data.

References

[1] Jens, E. T., Cantwell, B. J., and Hubbard, G. S., "Hybrid Rocket Propulsion Systems for Outer Planet Exploration Missions," *Acta Astronautica*, Vol. 128, Nov.–Dec. 2016, pp. 119–130. https://doi.org/10.1016/j.actaastro.2016.06.036

[2] Lengellé, G., Foucaud, R., Godon, J. C., Heslouin, A., Lecourt, R., and Maisonneuve, Y., "Hybrid Propulsion for Small Satellites Analysis and Tests," *35th AIAA/ASME/SAE/ASEE Joint Propulsion Conference & Exhibit*, AIAA Paper 1999-2321, 1999. https://doi.org/10.2514/6.1999-2321

[3] Chiaverini, M. J., and Kuo, K. K. (eds.), *Fundamentals of Hybrid Rocket Combustion and Propulsion*, Vol. 218, Progress in Aeronautics & Astronautics, AIAA, Reston, VA, 2007, Chap. 4. https://doi.org/10.2514/4.866876

[4] Korting, P. A. O. G., Schöyer, H. F. R., and Timnat, Y. M., "Advanced Hybrid Rocket Motor Experiments," *Acta Astronautica*, Vol. 15, No. 2, Feb. 1987, pp. 97–104. https://doi.org/10.1016/0094-5765(87)90009-9

[5] De Zilwa, S., Zilliac, G., and Reinath, M., "Time-Resolved Fuel-Grain Port Diameter Measurements in Hybrid Rockets," *Journal of Propulsion and Power*, Vol. 20, No. 4, July–Aug. 2004, pp. 684–689. https://doi.org/10.2514/1.2188

[6] Chiaverini, M. J., Serin, N., Johnson, D. K., Lu, Y.-C., Kuo, K. K., and Risha, G. A., "Regression Rate Behavior of Hybrid Rocket Solid Fuels," *Journal of Propulsion and Power*, Vol. 16, No. 1, Jan.–Feb. 2000, pp. 125–132. https://doi.org/10.2514/2.5541

[7] DeLuca, L. T., Galfetti, L., Colombo, G., Maggi, F., Bandera, A., Boiocchi, M., Gariani, G., Merotto, L., Paravan, C., and Reina, A., "Time-Resolved Burning of Solid Fuel for Hybrid Rocket Propulsion," *Progress in Propulsion Physics*, Vol. 2, 2011, pp. 405–426. https://doi.org/10.1051/eucass/201102405

[8] Narsai, P., "Nozzle Erosion in Hybrid Rocket Motors," Ph.D. Thesis, Stanford Univ., Stanford, CA, 2016.

[9] Mechentel, F. S., and Cantwell, B. J., "Small-Scale Gaseous Oxygen Hybrid Rocket Testing Facility Upgrades for Regression Rate and Combustion Efficiency Studies," *2018 Joint Propulsion Conference*, AIAA Paper 2018-4439, 2018. https://doi.org/10.2514/6.2018-4439

[10] Mechentel, F. S., "Preliminary Design of a Hybrid Motor for Small-Satellite Propulsion," Ph.D. Thesis, Stanford Univ., Stanford, CA, 2019.

[11] Bywater, S., and Toporowski, P. M., "Effect of Stereostructure on Glass Transition Temperatures of Poly(methyl methacrylate)," *Polymer*, Vol. 13, No. 3, 1972, pp. 94–96. https://doi.org/10.1016/S0032-3861(72)80001-6

[12] Michel, P., Dugas, J., Cariou, J. M., and Martin, L., "Thermal Variations of Refractive Index of PMMA, Polystyrene, and Poly(4-methyl-1-pentene)," *Journal of Macromolecular Science*, Vol. 25, No. 4, 1986, pp. 379–394. https://doi.org/10.1080/00222348608248046

[13] Karabeyoglu, M. A., "Transient Combustion in Hybrid Rockets," Ph.D. Thesis, Stanford Univ., Stanford, CA, 1998.

[14] Shlensky, O. F., Matyukhin, A. A., and Vaynshteyn, E. F., "Limiting Temperatures of the Thermal Decomposition of Polymers and Their Determination by Rapid Thermal Analysis," *Journal of Thermal Analysis*, Vol. 31, No. 1, 1986, pp. 107–115. https://doi.org/10.1007/BF01913891

[15] Kumar, R., and Ramakrishna, P. A., "Enhancement of Hybrid Fuel Regression Rate Using a Bluff Body," *Journal of Propulsion and Power*, Vol. 30, No. 4, 2014, pp. 909–916. https://doi.org/10.2514/1.B34975

[16] Carmicino, C., and Russo Sorge, A., "Performance Comparison Between Two Different Injector Configurations in a Hybrid Rocket," *Aerospace Science and Technology*, Vol. 11, No. 1, 2007, pp. 61–67. https://doi.org/10.1016/j.ast.2006.08.009

[17] Gramer, D. J., and Taagen, T. J., "Low-Cost Surface Regression Sensor for Hybrid Fuels, Solid Propellants and Ablatives," *37th AIAA/ASME/SAE/ASEE Joint Propulsion Conference & Exhibit*, AIAA Paper 2001-3529, 2001. https://doi.org/10.2514/6.2001-3529

[18] Marxman, G. A., Wooldridge, C. E., and Muzzy, R. J., "Fundamentals of Hybrid Boundary-Layer Combustion," *Progress in Astronautics and Rocketry*, Vol. 15, Jan. 1964, pp. 485–522. https://doi.org/10.1016/B978-1-4832-2730-6.50025-7

[19] Cantwell, B. J., "Similarity Solution of Fuel Mass Transfer, Port Mass Flux Coupling in Hybrid Propulsion," *Journal of Engineering Mathematics*, Vol. 84, No. 1, 2014, pp. 19–40. https://doi.org/10.1007/s10665-013-9624-y

[20] Mechentel, F. S., and Cantwell, B. J., "Experimental Findings on Pre- and Post-combustion Chamber Effects in a Laboratory-Scale Motor," *AIAA Propulsion and Energy 2019 Forum*, AIAA Paper 2019-4336, 2019. https://doi.org/10.2514/6.2019-4336

E. L. Petersen
Associate Editor